Transient Thermomechanical Analysis of Sliding Electrical Contacts of Elastoplastic Bodies, Thermal Softening, and Melting Inception

W. Wayne Chen

Q. Jane Wang

Department of Mechanical Engineering,
Northwestern University,
Evanston, IL 60208

Wansik Kim

Memory Division,
Semiconductor Business,
Samsung Electronics Co. LTD.,
San#16 Banwol-Dong, Hwansung-City,
Gyeonggi-Do 445-701, South Korea

Sliding electrical contacts are found in many electromechanical devices, such as relays, switches, and resistance spot welding. Temperature rise due to sliding friction and electrical current may be the major source of sliding electrical contact deterioration. This paper reports the development of a three-dimensional thermo-elasto-plastic contact model of counterformal bodies, which takes into account transient heat flux, temperature-dependent strain hardening behavior, and a realistic heat partition between surfaces. Transient contact simulations induce a significant increase in computational burden. The discrete convolution and fast Fourier transform and the conjugate gradient method are utilized to improve the computation efficiency. The present model is used to study the case of a half-space sliding over a stationary sphere, and both are made of 7075 aluminum alloy; the contact resistance is considered mainly due to the surface oxide film. The simulation results indicate that the transient contact model is able to capture the history of plastic deformation accumulation and the material melting inception.
[DOI: 10.1115/1.3084214]

Keywords: sliding electrical contact, elastoplasticity, thermal softening

1 Introduction

Sliding electrical contact [1] involves electrical current passing through the contact area and the sliding friction between two surfaces under relative motion. Most of the dissipated energy is transformed into heat, which is responsible for temperature rise, thermal distortion, and thermally induced component failures, such as scuffing and seizure. The inelastic deformation due to plastic strain is another critical issue for component failure under severe conditions. The material strength degradation and surface thermal expansion due to temperature rise play important roles in the performance of thermo-elasto-plastic contacts. Thus, a fully coupled thermal and mechanical analysis is desired for a sliding electrical contact.

Johnson [2] gave an overview of thermoelastic contact studies in his well-known book. Carslaw and Jaegar [3] presented a transient analytical integral formula for the temperature rise on the surface of a half-space subjected to a moving surface heat flux. Transient thermomechanical models have been developed for contacts involving viscous and dry frictional heating [4–7]. The finite element method (FEM) has been widely used to investigate the thermo-elasto-plastic contacts [8–10]. FEM was also employed to calculate the generic thermal displacement and temperature solutions of a unit heat flux at the origin; these solutions may be used in a fast contact algorithm [11,12].

Joule heating is generated when electrical current passing through a surface involving electrical contact resistance (ECR). Thin insulating films formed at the contact interfaces cause the tunneling effect, which may be the major source of ECR. In the past decades, many researches have been performed to correlate film resistance with surface film thickness [1,13–15] and surface geometry parameters [16]. Incorporating the thermal effect caused by Joule heating, Kim et al. [17] conducted a FEM analysis of the electrical contacts involving imperfect rough surfaces. Moreover, a fast Fourier transform (FFT) based model [18] has been developed to simulate the steady-state and transient temperature rises under sliding electrical contact, and then later been used to compute rough surface melting of electrical contacts subjected to a high current density [19].

A semi-analytical method (SAM) [20–29] was introduced to solve contact problems involving elastoplasticity or thermal deformation. Wang and co-workers [20,21] proposed three-dimensional thermomechanical models of contacts with rough surface due to moving and stationary surface heat fluxes. Transient temperature and stress field in the semi-infinite space were derived by Liu and Wang [22] in terms of frequency response functions (FRFs) in the wave domain. Jacq et al. [23] developed a semi-analytical elasto-plastic contact model for counterformal contacts with smooth or dented surfaces. In addition, steady-state heat flux [24,25] has been introduced into the model in Ref. [23].

Reported in this paper is the development of a three-dimensional thermo-elasto-plastic contact model based on the formulations derived in Ref. [22] and the algorithm presented in Ref. [23]. The present model considers the transient heat conduction and temperature-dependent strain hardening. Transient three-dimensional simulations cause a dramatic increase in the computation time. The FFT algorithm [30–32] and the conjugate gradient method (CGM) [33] can help reduce the computational burden. A sliding electrical point contact is simulated by both the transient and steady-state models. The aluminum alloy Al7075 is studied. Surface pressure, temperature rise, and subsurface stress and strain evolutions with time are presented. Material melting inception time is also discussed for various magnitudes of the electrical current densities and the mechanical loads.

Contributed by the Tribology Division of ASME for publication in the JOURNAL OF TRIBOLOGY. Manuscript received May 6, 2008; final manuscript received December 30, 2008; published online March 6, 2009. Assoc. Editor: Andreas A. Polycarpou.

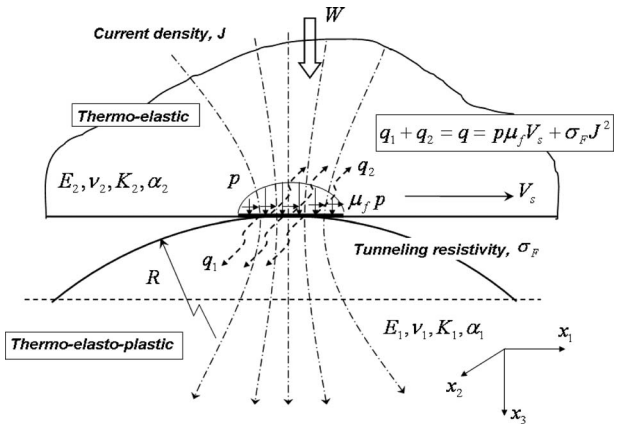

Fig. 1 Conceptual figure of the sliding electrical contact under frictional and Joule heating

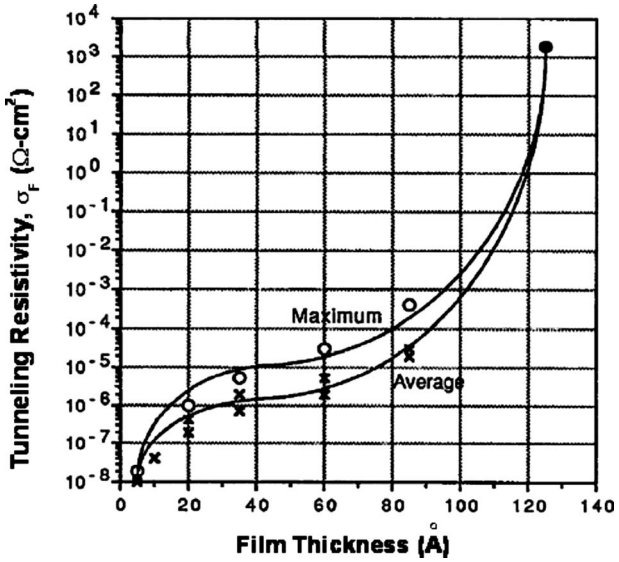

Fig. 2 Tunneling resistivity for TiO_2 film on Ti as a function of film thickness [13]

2 Theoretical Background

2.1 Sliding Electrical Contact and Tunneling Resistivity. Figure 1 illustrates a sliding electrical contact involving a moving half-space (Body 2) and a stationary sphere (Body 1). When two surfaces are brought into contact by a mechanical load, W, surface tractions are developed on the real contact area, and the electrical current lines become distorted and pass through the contact interface [1]. The thermal effect due to electrical Joule heating and frictional heating may induce severe thermoplastic deformation and remarkable temperature rise, which are responsible for the contact surface degradation.

Flowing of electrical current through an interface resistance causes energy transformation. ECR [1,34] can be categorized into three components: the constriction resistance, interaction resistance, and film resistance due to the electron tunneling effect. Thin insulating oxide films can be instantly formed when surfaces are exposed to normal atmosphere. The tunneling effect is referred to as the process of electron penetrating the potential barrier of an insulating film. It has been demonstrated that the film resistance is the dominant part of the ECR for most metal surfaces [15,16]. Kim [19] showed that the film resistance is about 99.9% of the total ECR on an aluminum surface. Thus, the constriction resistance and interaction resistance are neglected in this study for simplicity. The film resistance, R_F, is defined as

$$R_F = \frac{\sigma_F}{A_c} \tag{1}$$

where σ_F is the tunneling resistivity of the insulating film and A_c is the real contact area. Dietrich [14] developed a general curve of the tunneling resistivity for TiO_2 on Ti as a function of film thickness, as shown in Fig. 2. Although the curve in Fig. 2 was empirically derived for TiO_2, it is thought to be approximately applicable to most metallic materials [15]. In Sec. 3, the effect of tunneling resistivity is studied, and the applicability of using Fig. 2 to determine the tunneling resistivity between aluminum bodies is validated via the comparison of experimental and numerical results. Because the oxide film of Al_2O_3 is very thin, the contact analyses may be conducted based on the properties of the bulk material [16,35].

2.2 Heat Flux and Transient Thermomechanical Field. Heat generated in the sliding electrical contact raises the surface temperature, which causes thermal expansion and thermal stress. Suppose that all the energy dissipated is transformed to heat, which is distributed between two contacting solids. A sliding electrical contact may involve two major heat sources: Joule heating caused by electrical resistance and frictional heating as a result of relative motion. Thus, the total heat flux in a local contact area can be defined as

$$q = q_{\mathrm{Fri}} + q_{\mathrm{ECR}} = \mu_f p V_s + J^2 \sigma_F \tag{2}$$

Here, p is the local normal pressure, μ_f is the friction coefficient, V_s is the relative sliding velocity, and J is the current density (the current passing a unit area).

The temperature rise and the thermomechanical stress field in a half-space due to an irregularly distributed surface heat source were discussed by Liu and Wang [22] in terms of the FRF, which is the Fourier transform of Green's function. In order to present the formulations, several dimensionless variables are introduced: $\underline{T}=\alpha_t T$, $\underline{q}=q\alpha_t l/K$, $\underline{x}_i=x_i/l$, $\underline{u}_i=u_i/l(1+\nu)$, and $\underline{t}=t\kappa/l^2$, where T is temperature rise, q is heat flux, t is time, α_t is linear thermal expansion coefficient, K is thermal conductivity, κ is the thermal diffusivity, l is the characteristic length, and ν is the Poisson ratio. The Cartesian coordinates system (x_1,x_2,x_3) is shown in Fig. 1. The Péclet numbers Pe_1 and Pe_2 along two surface axes x_1 and x_2 are defined as $\mathrm{Pe}_1=V_1 l/\kappa$ and $\mathrm{Pe}_2=V_2 l/\kappa$ when the interface sliding velocities V_1 and V_2 are time-independent. The time-dependent surface heat flux $\underline{q}(\underline{x}_1,\underline{x}_2,\underline{t})$ ($\underline{q}=0$ for $\underline{t}<0$) causes a transient temperature rise, $\underline{T}(\underline{x}_1,\underline{x}_2,\underline{x}_3,\underline{t})$, inside the body, which induces a transient thermoelastic displacement, $\underline{u}_i(\underline{x}_1,\underline{x}_2,\underline{x}_3,\underline{t})$, in the x_i direction. The surface except the real contact area is assumed to be adiabatic; thus the model predicts the upper limit of interfacial temperature. The bulk temperature of the contact bodies at $\underline{t}=0$ equals the room temperature.

The temperature rise caused by a surface heat flux is derived by Carslaw and Jaeger [3] in the form of an integral equation. Applying the two-dimensional Fourier transform with respect to the x_1 and x_2 directions, the temperature rise of the half-space in a hybrid domain (frequency, depth, and time) is expressed by

$$\underline{\underline{\tilde{T}}}(m,n,\underline{x}_3,\underline{t}) = \int_0^{\underline{t}} \underline{\underline{\tilde{q}}}(m,n,t)\frac{1}{\sqrt{\pi(\underline{t}-\tau)}} \times \exp\left[-\frac{\underline{x}_3}{4(\underline{t}-\tau)} - (\underline{t}-\tau)w'^2\right] d\tau \tag{3}$$

where m and n are the frequency coordinates corresponding to

x_1 and x_2, $w=\sqrt{m^2+n^2}$, $a=i(m\cdot \mathrm{Pe}_1+n\cdot \mathrm{Pe}_2)$, $w'=\sqrt{w^2-a}$, and each "~" means a Fourier transform operation. The FRF of transient temperature rise due to a time-invariant surface heat flux, $\bar{\bar{q}}(m,n)$, was derived by Liu and Wang [22] as

$$\bar{\bar{G}}^{\Delta T}(m,n,\underline{x}_3,\underline{t})=\frac{\bar{\bar{T}}(m,n,\underline{x}_3,\underline{t})}{\bar{\bar{q}}(m,n)}=\begin{cases}\dfrac{1}{2w'}\left[\exp(-w'\underline{x}_3)\mathrm{erfc}\left(\dfrac{\underline{x}_3}{2\sqrt{\underline{t}}}-w'\sqrt{\underline{t}}\right)-\exp(w'\underline{x}_3)\mathrm{erfc}\left(\dfrac{\underline{x}_3}{2\sqrt{\underline{t}}}+w'\sqrt{\underline{t}}\right)\right], & w'\neq 0\\ 2\dfrac{\sqrt{\underline{t}}}{\sqrt{\pi}}\exp\left(-\dfrac{\underline{x}_3^2}{4\underline{t}}\right)-\underline{x}_3\,\mathrm{erfc}\left(\dfrac{\underline{x}_3}{2\sqrt{\underline{t}}}\right), & w'=0\end{cases} \tag{4}$$

where $\mathrm{erf}(\xi)=2/\sqrt{\pi}\int_0^{\xi}\exp(-\tau^2)d\tau$ and $\mathrm{erfc}(\xi)=2/\sqrt{\pi}\int_{\xi}^{\infty}\exp(-\tau^2)d\tau$ are error function and complementary error function, respectively.

The thermoelastic field in the half-space due to a surface heat flux is developed by Liu and Wang [22] following the approach of Seo and Mura [36]. The FRFs of the quasistatic normal surface displacement caused by the time-invariant heat flux is

$$\bar{\bar{G}}^{u_3}(m,n,0,\underline{t})=\frac{\bar{\bar{u}}_3(m,n,0,\underline{t})}{\bar{\bar{q}}(m,n)}=-2\int_0^{\underline{t}}\exp(a\tau)\mathrm{erfc}(w\sqrt{\tau})d\tau$$
$$=\begin{cases}\dfrac{2}{a}\left[1-\exp(a\underline{t})\mathrm{erfc}(w\sqrt{\underline{t}})-\dfrac{w}{w'}\mathrm{erf}(w'\sqrt{\underline{t}})\right], & a\neq 0,\quad w\neq 0\quad \text{(moving)}\\ -2\left[\underline{t}\,\mathrm{erfc}(w\underline{t})-\dfrac{\exp(-w^2\underline{t})\sqrt{\underline{t}}}{w\sqrt{\pi}}+\dfrac{\mathrm{erf}(w\underline{t})}{2w^2}\right], & a=0,\quad w\neq 0\quad \text{(stationary)}\\ -2\underline{t}, & w'=0\quad \text{(at origin)}\end{cases} \tag{5}$$

Using the double Fourier transform, Liu and Wang [22] derived the closed-form solutions of the thermoelastic stress in the stationary semi-infinite body ($a=0$) in the frequency domain, which are given as follows:

$$\bar{\bar{\sigma}}_{11}=c_m[-4\pi\bar{\bar{T}}+m^2\bar{\bar{\varphi}}^{\mathrm{I}}+((3-4\nu)m^2+4\nu w^2-2\underline{x}_3 wm^2)\bar{\bar{\varphi}}^{\mathrm{II}}]$$

$$\bar{\bar{\sigma}}_{22}=c_m[-4\pi\bar{\bar{T}}+n^2\bar{\bar{\varphi}}^{\mathrm{I}}+((3-4\nu)n^2+4\nu w^2-2\underline{x}_3 wn^2)\bar{\bar{\varphi}}^{\mathrm{II}}]$$

$$\bar{\bar{\sigma}}_{33}=c_m[-4\pi\bar{\bar{T}}-\bar{\bar{\varphi}}^{\mathrm{I}}_{,33}+(1+2\underline{x}_3 w)w^2\bar{\bar{\varphi}}^{\mathrm{II}}]$$

$$\bar{\bar{\sigma}}_{12}=c_m mn[\bar{\bar{\varphi}}^{\mathrm{I}}+(3-4\nu-2\underline{x}_3 w)\bar{\bar{\varphi}}^{\mathrm{II}}]$$

$$\bar{\bar{\sigma}}_{13}=ic_m m[-\bar{\bar{\varphi}}^{\mathrm{I}}_{,3}+(1-2\underline{x}_3 w)w\bar{\bar{\varphi}}^{\mathrm{II}}],$$

$$\bar{\bar{\sigma}}_{23}=ic_m n[-\bar{\bar{\varphi}}^{\mathrm{I}}_{,3}+(1-2\underline{x}_3 w)w\bar{\bar{\varphi}}^{\mathrm{II}}] \tag{6}$$

Here, $c_m=E/4\pi(1-\nu)$, E is Young's modulus, and subscript ",3" means partial derivative with respect to $\underline{x}_3$. $\bar{\bar{\varphi}}^{\mathrm{I}}$ and $\bar{\bar{\varphi}}^{\mathrm{II}}$ are the Fourier transforms of potential functions. $\bar{\bar{\varphi}}^{\mathrm{I}}$, $\bar{\bar{\varphi}}^{\mathrm{II}}$, and the derivatives of $\bar{\bar{\varphi}}^{\mathrm{I}}$ are given in the Appendix. Because the sphere radius is much larger than the contact area dimensions, the above equations, which are developed for a half-space, are also applicable for the sphere in this study. At the time of $\underline{t}=0$, the transient FRFs of the thermomechanical field vanish, while at the infinite time of $\underline{t}=\infty$, the transient FRFs can be reduced to the steady-state FRFs, which have already been shown in Ref. [25].

The FRFs derived above are for the cases with time-invariant surface heat flux. However, the heat flux may be a function of time because the contact area variation due to thermal distortion reversely alters the heat flux distribution. In order to account for the time-dependent heat flux, the total simulation time range, $\underline{t}$, is divided into N_t time intervals, and the ending time of the kth interval is $\underline{t}_k$ (i.e., $\underline{t}_3=0$ and $\underline{t}_{Nt}=\underline{t}$). Then the temperature rise in Eq. (3) can be written as a summation of integrals over discrete time intervals.

$$\bar{\bar{T}}(m,n,\underline{x}_3,\underline{t})=\sum_{k=1}^{N_t}\int_{\underline{t}_{k-1}}^{\underline{t}_k}\bar{\bar{q}}(m,n,\tau)M(\underline{t}-\tau)d\tau \tag{7}$$

where $M(\xi)=\exp(-\underline{x}_3/(4\xi)-\xi w'^2)/\sqrt{\pi\xi}$. The heat flux in each time interval is assumed to be constant, and then they can be factored out from the integrals

$$\bar{\bar{T}}(m,n,\underline{x}_3,\underline{t})=\sum_{k=1}^{N_t}\bar{\bar{q}}(m,n,\underline{t}_k)\int_{\underline{t}_{k-1}}^{\underline{t}_k}M(\underline{t}-\tau)d\tau \tag{8}$$

In order to make use of the FRFs for the time-invariant heat flux, $\bar{\bar{G}}^{\Delta T}$, further manipulation is done to Eq. (8) to change the upper limits of integrals to the total simulation time, $\underline{t}$

$$\bar{\bar{T}}(m,n,\underline{x}_3,\underline{t})=\sum_{k=1}^{N_t}\bar{\bar{q}}(m,n,\underline{t}_k)\left[\int_{\underline{t}_{k-1}}^{\underline{t}}M(\underline{t}-\tau)d\tau-\int_{\underline{t}_k}^{\underline{t}}M(\underline{t}-\tau)d\tau\right]$$
$$=\sum_{k=1}^{N_t}[\bar{\bar{q}}(m,n,\underline{t}_k)-\bar{\bar{q}}(m,n,\underline{t}_{k-1})]\int_{\underline{t}_{k-1}}^{\underline{t}}M(\underline{t}-\tau)d\tau \tag{9}$$

Using the variable substitution of $\eta=\tau-\underline{t}_{k-1}$, one has

$$\bar{\bar{T}}(m,n,\underline{x}_3,\underline{t})=\sum_{k=1}^{N_t}[\bar{\bar{q}}(m,n,\underline{t}_k)-\bar{\bar{q}}(m,n,\underline{t}_{k-1})]\int_0^{\underline{t}-\underline{t}_{k-1}}M(\underline{t}-\underline{t}_{k-1}-\eta)d\eta=\sum_{k=1}^{N_t}[\bar{\bar{q}}(m,n,\underline{t}_k)-\bar{\bar{q}}(m,n,\underline{t}_{k-1})]\bar{\bar{G}}^{\Delta T}(m,n,\underline{x}_3,\underline{t}-\underline{t}_{k-1}) \tag{10}$$

Here, $\bar{\bar{q}}(m,n,\underline{t}_0)=0$ is from the initial condition. The inverse FFT (IFFT) algorithm is used to convert the known frequency response functions to influence coefficients in the space domain, which are needed in thermomechanical contact simulations. The detailed process was described in Ref. [32].

Instead of assuming that heating is evenly partitioned between the two bodies or solely absorbed by one body regardless of the interfacial temperature distribution, a deterministic scheme [4,25]

is employed to calculate the amount of heat flowing into each contact body. The generated heat is partitioned so as to assure that the temperature rises on the two surfaces at corresponding contact points are the same.

2.3 Contact Modeling. An unlubricated normal contact is governed by the following equations:

$$W = \int_{A_c} p(x_1,x_2) \cdot dx_1 dx_2 \tag{11}$$

$$h(x_1,x_2) = h_i(x_1,x_2) + u_3(x_1,x_2) - \delta \geq 0 \tag{12}$$

where A_c is the real contact area, u_3 is the combined normal displacement of two bodies, h_i is the initial surface geometry ($h_i = (x_1^2 + x_2^2)/2R$ for the sphere of radius R), and h and δ are the surface gap and the rigid body approach, respectively. The normal displacement has three sources: the elastic deformation due to surface normal and shear tractions, the residual one due to plastic strain, and the thermal one due to heating.

The elastic displacement caused by surface tractions can be calculated with the Boussinesq–Cerruti integrals [2]

$$u_3(x_1,x_2) = \int_{-\infty}^{\infty}\int_{-\infty}^{\infty} [G^p(x_1 - \xi, x_2 - \eta) + \mu_f \cdot G^s(x_1 - \xi, x_2 - \eta)]p(\xi,\eta)d\xi d\eta \tag{13}$$

Here, G^p and G^s are Green's functions for pressure and shear traction, whose formula can be found in Ref. [20]. General solutions of displacements due to uniform tractions over the element at the origin (i.e., influence coefficients) can be obtained by integrating the corresponding Green's function [31]. The evaluation of residual displacement was presented by Jacq et al. [23] based on the reciprocal theorem, and the approach to obtaining the influence coefficients of thermal displacements on the moving and stationary contact bodies is given in Sec. 2.2.

Analyzing such a contact problem is essentially a process of solving a linear equation system with the unknown pressure distribution. Thus, a single-loop conjugate gradient method [33] is used to find surface pressure and the real contact area. In addition, the discrete convolution and fast Fourier transform (DC-FFT) algorithm presented in Ref. [32] is introduced to accelerate computational efficiency.

Determination of subsurface stresses is a necessary step toward the understanding of the plastic deformation evolution. The computation of the elastic stress field in a half-space caused by irregularly distributed surface tractions (normal and shear) is based on the method of Liu and Wang [37] with the influence coefficients derived by Love [38]. The approach of Jacq et al. [23] for the stresses due to the distributed plastic strain, which is based on a general solution of uniform eigenstrain in a cubic zone in Ref. [39], is utilized for the residual stress simulation. In addition, the solution of transient thermoelastic stress due to surface heat flux (listed in Sec. 2.2) by Liu and Wang [22] is used for thermal stress analysis.

2.4 Plasticity Considering the Thermal Softening Effect. The compressive stress-strain response of 7075 aluminum alloy has been investigated by Lee et al. [40] experimentally under different temperatures. A temperature-dependent strain hardening behavior can be derived from the experimental results

$$g(\lambda) = B(C + \lambda)^e(1 - \beta \cdot \Delta T) \tag{14}$$

Here, g is the strain hardening function, and $g(0)$ equals the initial yield strength, $\sigma_Y = 503.24$ MPa. $\lambda = \Sigma d\lambda = \Sigma(\sqrt{2 d\varepsilon_{ij}^p d\varepsilon_{ij}^p}/3)$ is the effective accumulative plastic strain, and $d\varepsilon_{ij}^p$ is the plastic strain increment tensor. The strain hardening parameters are $B = 867.9$ MPa, $C = 3.3 \times 10^{-4}$, and $e = 0.068$. The thermal softening coefficient is $\beta = 1.35 \times 10^{-3}$ K^{-1}. $\Delta T = T - T_0$ is the temperature rise and T_0 is the room temperature.

The J-2 criterion [41] (valid for most metal materials) in Eq. (15) is used to determine the onset of material yield

$$f = \sigma_{VM} - g(\lambda) = \sqrt{\tfrac{3}{2} S_{ij} : S_{ij}} - g(\lambda) \tag{15}$$

Here, σ_{VM} is the von Mises equivalent stress, and $S_{ij} = \sigma_{ij} - \sigma_{kk}\delta_{ij}/3$ is the deviatoric stress (σ_{ij} is the Cauchy stress tensor and δ_{ij} is the Kronecker delta function). Yielding occurs when the von Mises equivalent stress (square root of J-2 invariant of stress tensor) exceeds the local yield strength stated in Eq. (14) corresponding to the updated effective plastic strain and temperature rise (i.e., $f > 0$). The actual increment of the effective plastic strain, $d\lambda$, should be the value that satisfies the condition $f(\lambda + d\lambda) = 0$. The plastic strain increment reversely changes the contact surface geometry; the surface contact has to be resimulated to update surface pressure and heat flux distributions. Therefore, the effective plastic strain increment is found by an iterative process [23]. Consequently, the variation of the plastic strain tensor is calculated in the light of the plastic flow rule [41] shown in

$$d\varepsilon_{ij}^p = d\lambda \frac{3S_{ij}}{2\sigma_{VM}} \tag{16}$$

3 Results and Discussion

The present model has been used to analyze the sliding electrical contact involving a moving half-space and a stationary sphere, whose radius is $R = 8$ mm. In order to simplify the numerical work, the sphere is considered to be fully thermo-elasto-plastic, while the mating surface is assumed to thermo-elastic. Materials of the two contact bodies are the same and have the properties of 7075 aluminum alloy. Simulation results of surface pressure, temperature rise, and subsurface stress and strain evolutions in the sphere body are presented in this section. The maximum dimensionless load is $W/W_c = 2.56$ ($W = 300$ N), where W_c is the critical normal load indicating the transition from an elastic contact to an elastoplastic one under the mechanical load alone [42]

$$W_c = \frac{(\pi\Lambda)^3}{6}\left(\frac{H}{E^*}\right)^2 HR^2 \tag{17}$$

In the equation above, $1/E^* = \Sigma_{i=1}^2 1 - \nu_i^2/E_i$, H is the material hardness, and Λ is the hardness coefficient related to the Poisson ratio by $\Lambda = 0.454 + 0.41\upsilon$. The Hertz solutions of contact radius a_0 and peak pressure p_0 are used to normalize the coordinates and contact pressure; and their definitions are

Table 1 Simulation parameters and material properties of Al7075 alloy

Young's modulus, E (GPa)	71.7
Poisson ratio, ν	0.33
Yield strength, σ_Y (MPa)	503.24
Strain hardening parameter, B (MPa)	867.9
Strain hardening parameter, C	3.3×10^{-4}
Strain hardening exponent, e	0.068
Thermal conductivity, K (W/m K)	130
Thermal expansion coefficient, α_t (μm/m K)	25.2
Thermal diffusivity, κ (m^2/s)	5×10^{-5}
Characteristic length, l (mm)	1
Thermal softening coefficient, β (K^{-1})	1.35×10^{-3}
Melting incipient point, T_m (K)	805
Room temperature, T_0 (K)	300
Sphere radius, R (mm)	8
Friction coefficient, μ_f	0.1
Péclet number, Pe_1	10
Normal load, W (N)	300
Tunneling resistivity, σ_F (Ω mm^2)	0.1
Current density, J (A/mm^2)	≤ 120

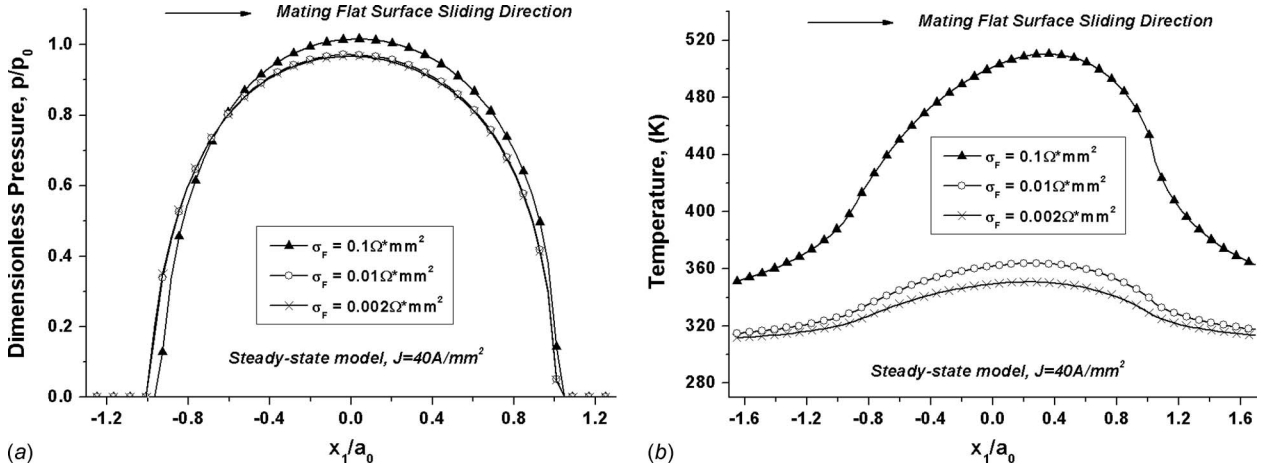

Fig. 3 Simulation results using different tunneling resistivities (J=40 A/mm^2), (*a*) pressure along the axis of symmetry, and (*b*) temperature along the axis of symmetry

$$a_0 = \sqrt[3]{3WR/4E^*}, \quad p_0 = \frac{1}{\pi}\sqrt[3]{6WE^{*2}/R^2} \tag{18}$$

The friction coefficient is μ_f=0.1, and the Péclet numbers are Pe_1=10 and Pe_2=0. Electrical current density up to J =120 A/mm^2 is applied in the simulations. Material mechanical and thermal properties and simulation parameters are summarized in Table 1.

In Fig. 2, the tunneling resistivity is very sensitive to the surface film thickness, and its value may vary from 0.002 Ω mm^2 (80 Å) to 0.1 Ω mm^2 (100 Å). Note that the unit of tunneling resistivity in Fig. 2 is Ω cm^2. In this paper, the tunneling resistivity curve of TiO_2 is used approximately to obtain the tunneling resistivity of Al_2O_3. Therefore, studies on the effects of tunneling resistivity on temperature and contact pressure are carried out, and the results are presented in Fig. 3. The tunneling resistivity has a relatively small influence on pressure especially when the tunneling resistivity is below 0.01 Ω mm^2 and has a remarkable influence on the temperature rise. The temperature rise at σ_F =0.1 Ω mm^2 is five times larger than that at σ_F=0.002 Ω mm^2. It was found that Al_2O_3 films on Al tend to stop growing after reaching a thickness of about 50 Å [1], which implies that the insulating films formed between two aluminum components are about 100 Å in thickness. Thus, the tunneling resistivity of σ_F =0.1 Ω mm^2 is used in this paper for the contact of Al_2O_3 bodies. In order to justify the selection of tunneling resistivity, the numerical result of temperature rise is compared with the experimental measurement in Ref. [43] for an electrical contact between two aluminum parts. In the experiments in Ref. [43], the average pressure was 4.39 MPa and the current density was 1.89 A/mm^2. The pressure in the numerical simulation is set equal to 4.39 MPa to mimic the mechanical loading condition in the experiment. The temperature rise measured in the experiment was 0.4 K when the electrical current had been applied for 25 s. The average temperature rise in the contact area predicted by the steady-state numerical model is 0.6 K, which is in the same magnitude of the experimental data. The reasons for the difference could be that the films formed on the specimens were nonuniform, and that the temperature in the experiment did not rise to the final steady-state value.

The mechanical loading process is divided into 20 steps, where the normal load increases gradually from zero to its maximum. There are two possible schemes to applying the heat sources: (1) The thermal loading is applied after the mechanical loading reaches the peak value, and (2) the thermal and mechanical loadings are applied at the same time. Figure 4 compares the results obtained from the two loading schemes. It turns out that the results from the two schemes are very close; the maximum relative differences are 1.2% for contact pressure and 0.1% for temperature. Loading scheme 1 is used in the following analyses in order to better demonstrate the effects of thermal and mechanical loadings separately.

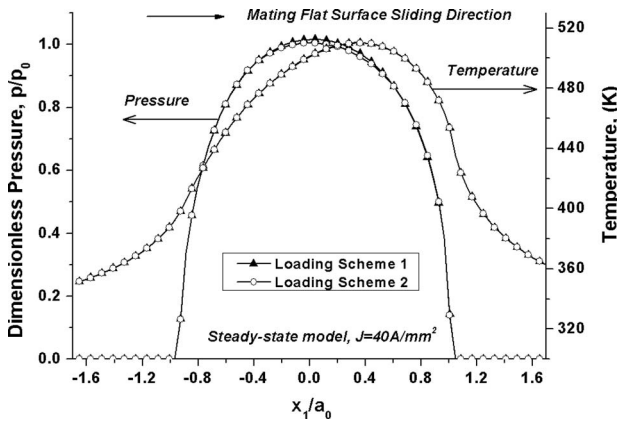

Fig. 4 Comparison of simulation results obtained from different loading schemes (J=40 A/mm^2)

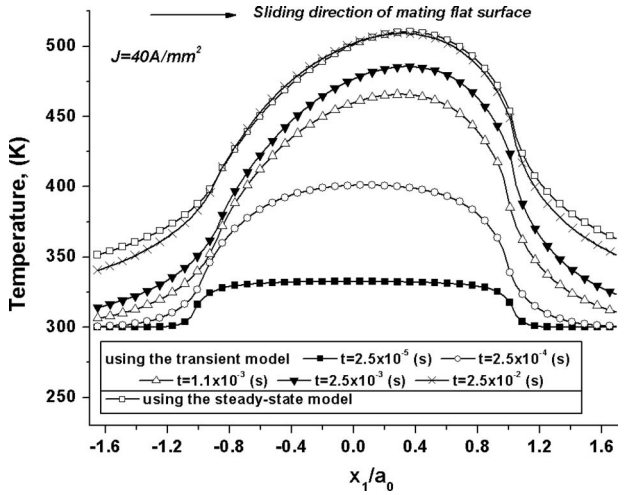

Fig. 5 Evolutions of temperature profiles along the axis of symmetry (J=40 A/mm^2)

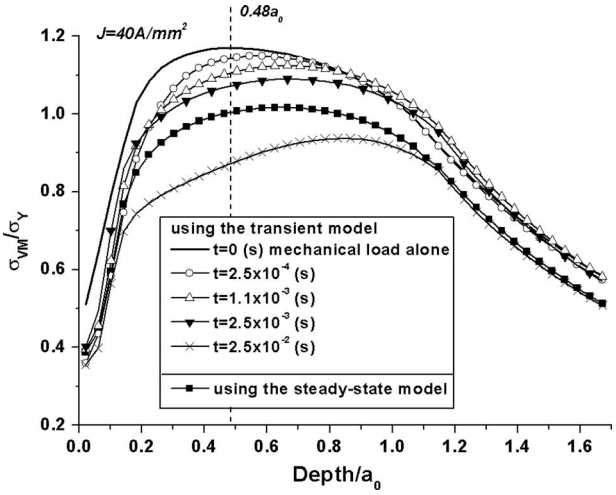

Fig. 6 Evolution of the equivalent von Mises stress along the depth (J=40 A/mm^2)

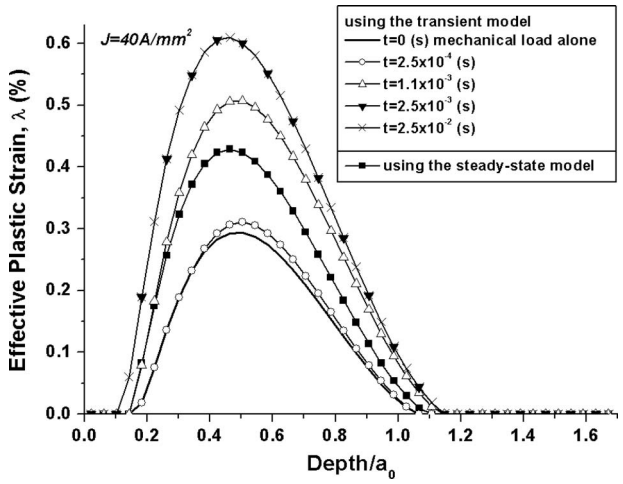

Fig. 8 Evolution of the effective plastic strain along the depth (J=40 A/mm^2)

Simulation results from the transient and steady-state models are shown in Figs. 5–9 when the current density is $J=40$ A/mm^2. Figure 5 gives the surface temperature distributions along the x_1 axis obtained from the steady-state and the transient models at different times. The surface temperature increases gradually with time. At the early stage of the simulation, only the area immediately beneath the contact experiences the temperature rise because the heat is unable to diffuse into the surrounding area in such a short time period. The maximum temperature from the transient analysis at $t=2.5\times10^{-2}$ s is 509.29 K, which is very close to the maximum temperature of 510.36 K from the steady-state model (relative difference less than 0.2%). It indicates that the heat conduction becomes stable and temperature rise at $t=2.5\times10^{-2}$ s converges to that from the steady-state model. This time may be treated as the stability time of the transient analyses. In addition, the maximum temperature position is shifted along the sliding direction.

Due to the thermal softening effect, high temperature rise deteriorates the material strength and reduces the maximum stress level that a material can sustain. The subsurface von Mises stresses along the depth from the transient and the steady-state models are presented in Fig. 6. Here, the stress is normalized by the yield strength, σ_Y. For an elastic frictionless Hertzian contact, the theoretical maximum von Mises stress occurs at the depth of $0.48a_0$. The von Mises stress at this depth decreases with time as expected. The depth of the maximum von Mises stress increases as the thermal contribution becomes more significant. A larger drop of the von Mises stress is detected in the zone near the surface because this zone involves a higher temperature rise than the deeper zone. In addition, the stress intensity from the transient model at the stability time of 2.5×10^{-2} s is lower than that from the steady-state model.

Figure 7 shows transient contact pressure profiles along the axis of symmetry at different times and also the steady-state pressure profile. Figure 8 shows the history of the subsurface effective plastic strain along the depth at the origin and the steady-state result. An interesting observation is that the contact pressure from the transient model first increases above the steady-state pressure, and then drops below the latter as the time increases. As shown in Fig. 8, the plastic strain obtained from the transient model experiences a more than twofold increase after the heat is applied, and is much higher than that from the steady-state model. The difference is likely due to the fact that the plastic deformation is by nature nonlinear and loading-history dependent. On the other hand, the steady-state thermomechanical model is history independent and can hardly handle a process involving thermal plasticity accumulation. More explanation and evidence will be given

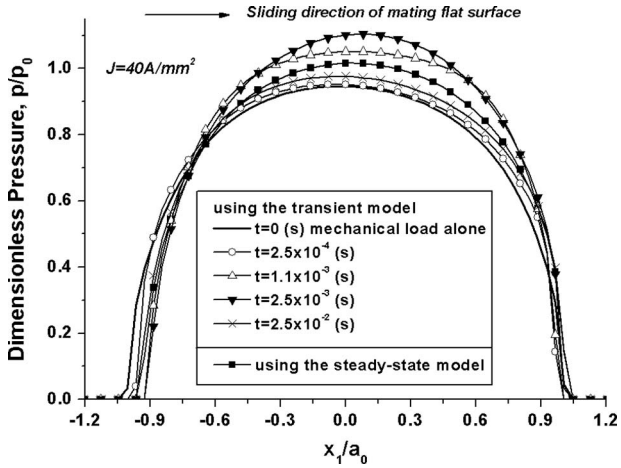

Fig. 7 Evolution of surface pressure along the axis of symmetry (J=40 A/mm^2)

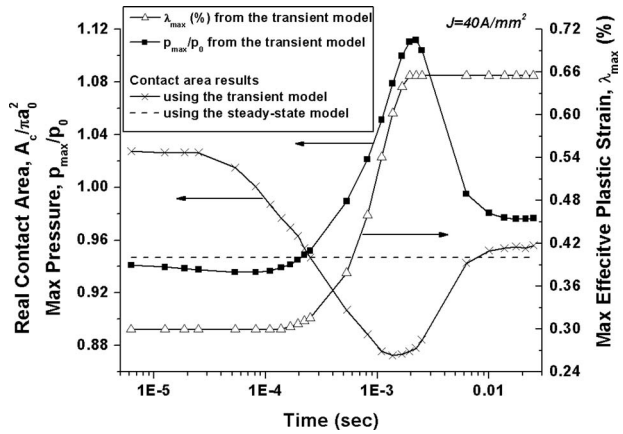

Fig. 9 Transient maximum pressure, maximum effective plastic strain, and the real contact area as functions of time (J =40 A/mm^2)

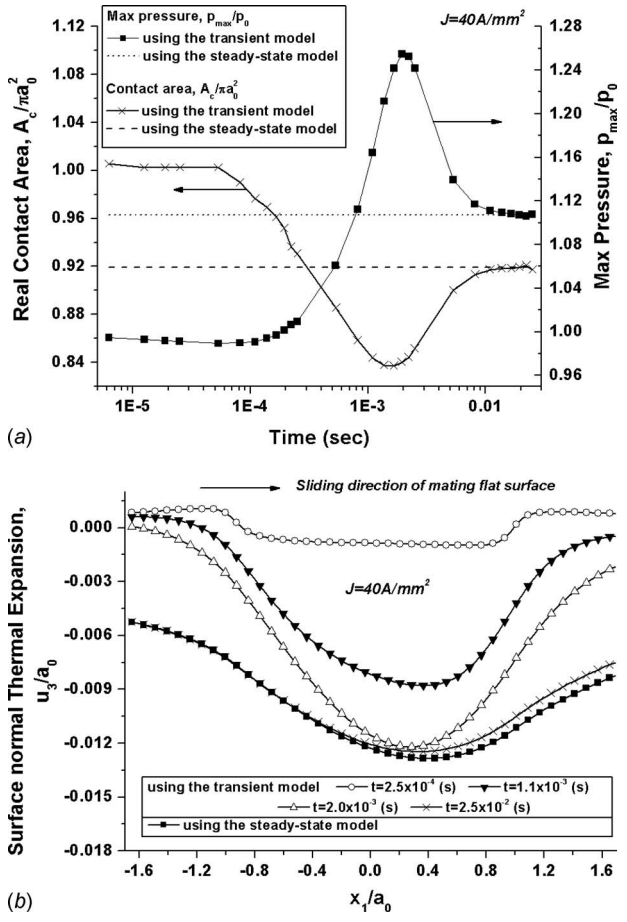

Fig. 10 Results for the thermo-elastic contact ($J=40$ A/mm^2), (*a*) maximum pressure and the real contact area as functions of time, and (*b*) evolution of the normal displacement along the axis of symmetry due to thermal expansion

in the following discussions. Another interesting point is that the transient plastic strain becomes stable earlier than stress, pressure, and temperature.

Figure 9 summarizes the variations of the peak contact pressure, the maximum subsurface effective plastic strain, and the real contact area as functions of time. The contact area shows a reversed tendency as compared with the contact peak pressure. The contact area at the stability time predicted by the transient model is larger than that by the steady-state model. This can explain why the transient peak pressure at the stability time drops below the steady-state peak pressure. It makes sense that the larger load bearing area leads to a smaller contact pressure. The peak pressure and the maximum plastic strain reach the maximum values at the same time (about $t=2\times10^{-3}$ s). The pressure drops after that moment, while the plastic deformation is irreversible and maintains its peak value.

The reason why the contact pressure shows such a nonmonotonic transitional trend with time may be attributed to the transient thermal expansion. In order to exclude the influence of plasticity and thermal softening, a thermo-elastic contact simulation was conducted using the same material properties and loading conditions, and the results are presented in Fig. 10. Figure 10(*a*) shows the variations of the peak contact pressure and the real contact area as functions of time. The same tendencies of the peak pressure and the real contact area are found as those in Fig. 9. It indicates that the thermal expansion has the dominant effect on the transient variation of the contact pressure and real contact area. Evolution of the normal displacement due to thermal expansion is also presented in Fig. 10(*b*). Because the temperature rise

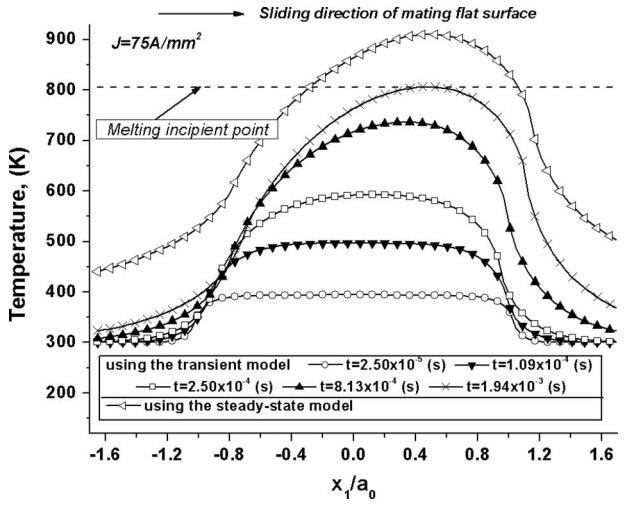

Fig. 11 Melting inception time identification using the transient model ($J=75$ A/mm^2)

is governed by the time-dependent Fourier equation, the thermal deformation caused by the temperature gradient lags behind the thermal loading [7]. At the early stage, heat is unable to diffuse into the surrounding area; and the surface thermal expansion mainly occurs at the area immediately next to the contact region. The concentrated thermal distortion increases the curvature of the surface geometry and enhances contact intensity. The thermally induced geometry distortion increases to the most severe state at the time of about $t=2\times10^{-3}$ s; thus the contact pressure reaches the maximum value at that moment. When heat conduction becomes stable, the surface at the surrounding area is uplifted due to the lagged thermal expansion, which alleviates surface contact severity and lowers the pressure. In contrast, the steady-state model cannot consider the transient variation process of surface geometry caused by thermal expansion.

Another advantage of the transient model over the steady-state model is that the former can identify the melting inception time under the application of a high electrical current density. Figure 11 gives the transient temperature distributions along the x_1 axis and the steady-state one when a current density of $J=75$ A/mm^2 is applied. The peak temperature predicted by the steady-state model is 910.38 K, which is higher than the material incipient melting point (805 K). A more sophisticated model incorporating phase transfer has to be used to capture the material behavior when the temperature is higher than the melting point. In order to identify the melting initiation time, the transient analysis has to be performed instead of the steady-state one. As illustrated in Fig. 11, at the time of about $t=1.94\times10^{-3}$ s, the maximum temperature at the surface reaches the Al7075 alloy's incipient melting temperature, which suggests that melting wear may occur within a short time interval of the millisecond order on the surface of such a sliding electrical contact (with $J=75$ A/mm^2) involving the Al7075 contact pairs.

Effects of the electrical current density and mechanical load on the material melting inception time are presented in Fig. 12. As indicated in Fig. 12(*a*), the melting inception time decreases significantly with the increase in electrical current density. The melting inception time drops almost two orders of magnitude (10–0.125 ms) when the applied current density increases from 70 A/mm^2 to 120 A/mm^2. One of the reasons is that the heat flux is proportional to the square of current density. In addition, the aforementioned thermal energy concentration phenomenon at the initial stage is more obvious in the higher current density case, and the interfacial heat is almost all absorbed by the material in and just beneath the contact area within a short time. Thus, the temperature rise in a higher current density case is much faster

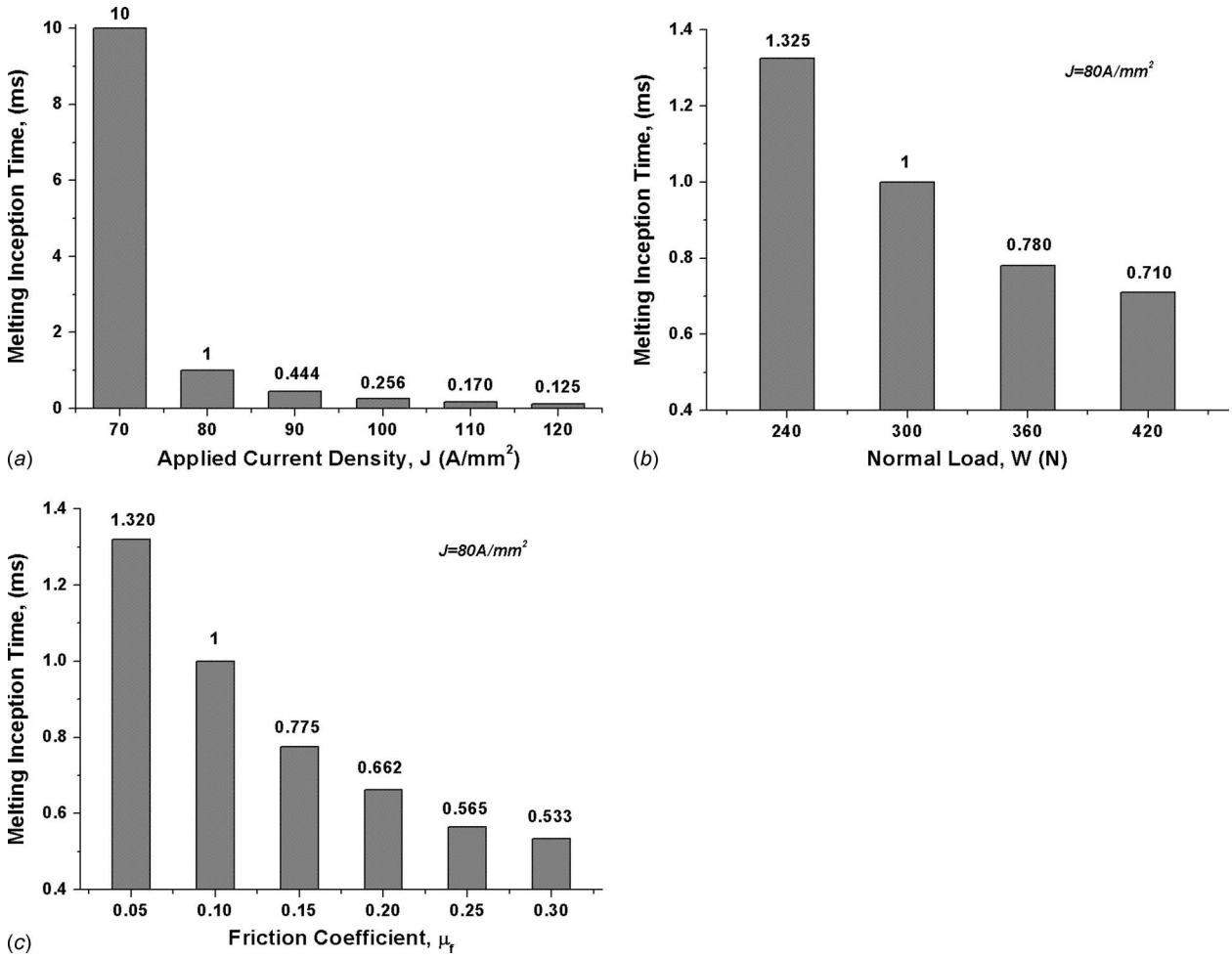

Fig. 12 Melting inception time variation with (*a*) the increase in electrical current density, (*b*) the increase in normal load, and (*c*) the increase in friction coefficient

than that in a lower current density case. Figures 12(*b*) and 12(*c*) show that the melting inception time decreases with the increase in normal load or the increase in friction coefficient. A larger normal load can lead to higher surface tractions (causing more frictional heating) and a larger contact area (resulting in a stronger electrical heat source for the case with a given current density). On the other hand, the increase in contact area expedites heat transfer, which lowers temperature. The results indicate that under the conditions analyzed in this study, the effect of strengthening heat source outweighs the effect of faster heat conduction. A larger friction coefficient leads to a higher surface shear traction that causes more energy dissipation and larger temperature rise.

4 Conclusions

A transient three-dimensional sliding thermo-elasto-plastic model has been developed for nonconformal contacts involving Joule and frictional heating. Transient thermomechanical analyses were conducted for the sliding electrical point contact of an Al7075 alloy contact pair. The results of transient pressure, temperature, and subsurface stress and strain are presented, and those predicted with the steady-state model are also shown for the purpose of comparison.

The transient model can well capture the histories of contact pressure, temperature, and subsurface stress. The analysis reveals a remarkable influence of transient heat transfer on plastic strain because of the dependence of plasticity on loading history. The accumulative plastic strain predicted by the transient model is larger than that by the steady-state model. The transient model is capable of identifying the inception melting time under a high electrical current density. Melting wear may occur at the electrical contact surfaces of the Al7075 alloy within a short time of the order of millisecond under the current density of about $J = 75\ \mathrm{A/mm^2}$. A shorter melting inception time may be achieved under an even larger electrical current density, a larger normal load, or a higher friction coefficient.

Acknowledgment

Research supports from the U.S. Office of Naval Research and Department of Energy are sincerely acknowledged. The authors would also like to thank Dr. Shuangbiao Liu in Caterpillar Inc. for helpful discussions.

Nomenclature

Roman Letters

a_0, p_0 = Hertz contact radius (mm) and peak pressure (MPa)
a = $i(m \cdot \mathrm{Pe}_1 + n \cdot \mathrm{Pe}_2)$
A_c = real contact area, mm^2
B, C, e = isotropic strain hardening law parameters, B (MPa)
c_m = $E/4\pi(1-\nu)$, MPa
E_i = Young's modulus two contact bodies, $i=1$ and 2

E^* = equivalent Young's modulus, GPa, $1/E^* = \Sigma_{i=1}^{2}(1-\nu_i^2)/E_i$
$g(\lambda)$ = strain hardening function, MPa
G = Green's functions
h, h_i = surface gap and initial gap, mm
H = hardness, GPa
J = electrical current density, A/mm^2
K = thermal conductivity, W/m K
l = characteristic length, mm
m, n = frequency domain coordinates corresponding to x and y
p = pressure and shear traction, MPa
Pe_1, Pe_2 = Péclet numbers along two axes
q = total heat flux, W/m^2
R = radius of the spherical body, mm
R_F = film resistance, Ω
S_{ij} = deviatoric stress, MPa, $S_{ij} = \sigma_{ij} - \sigma_{kk}\delta_{ij}/3$
t = time, s
T = temperature, K
T_m, T_0 = material incipient melting point and the room temperature, K
u_3 = surface normal displacement, mm
V_s = sliding velocity, m/s
w = distance in the frequency domain, $w = \sqrt{m^2+n^2}$
w' = effective distance in the frequency domain, $w' = \sqrt{w^2-a}$
W = normal load, N
x_1, x_2, x_3 = space coordinates, mm

Greek Letters

α_t = linear thermal expansion coefficient, μm/m K
β = thermal softening coefficient, K^{-1}
δ = rigid body approach, mm
ε_{ij}^p = plastic strain tensor
κ = thermal diffusivity, m^2/s
$d\lambda, \lambda$ = effective plastic incremental and accumulative strains
μ_f = friction coefficient
ν_i = Poisson ratio of two contact bodies, $i=1$ and 2
σ_{ij} = Cauchy stress tensor, MPa
σ_{VM} = von Mises equivalent stress, MPa
σ_Y = initial yield strength, MPa
σ_F = tunneling resistivity, Ω mm^2
ϕ^{I}, ϕ^{II} = Newtonian potentials used in thermal stress formulations

Special Marks

(), = partial differential operator
~ = Fourier transform operator

Appendix

The following equations are the potential functions $\tilde{\tilde{\varphi}}^{I}$ and $\tilde{\tilde{\varphi}}^{II}$, used in the thermomechanical stress formulation:

$$\tilde{\tilde{\varphi}}^{I} = \begin{cases} \dfrac{2\pi}{w}\tilde{\tilde{q}}\left[\gamma_1\left(\underline{t} + \dfrac{w\underline{x}_3 - 1}{2w^2}\right) + \gamma_2\left(\underline{t} - \dfrac{w\underline{x}_3 + 1}{2w^2}\right) - \dfrac{\gamma_4}{w} + \exp(-w\underline{x}_3)\left(\dfrac{w\underline{x}_3 + 1}{w^2} - \gamma_3\right)\right], & w \neq 0 \\ \dfrac{2\pi\underline{t}}{w}\tilde{\tilde{q}}[2 - \exp(-w\underline{x}_3)], & w = 0 \end{cases}$$

$$\tilde{\tilde{\varphi}}^{II} = \begin{cases} \dfrac{2\pi}{w}\tilde{\tilde{q}}\exp(-w\underline{x}_3)\gamma_3, & w \neq 0 \\ \dfrac{2\pi\underline{t}}{w}\tilde{\tilde{q}}\exp(-w\underline{x}_3), & w = 0 \end{cases}$$

$$\tilde{\tilde{\varphi}}^{I}_{,3} = \begin{cases} \dfrac{2\pi}{w}\tilde{\tilde{q}}\left[\gamma_1\left(w\underline{t} + \dfrac{\underline{x}_3}{2}\right) - \gamma_2\left(w\underline{t} - \dfrac{\underline{x}_3}{2}\right) + \exp(-w\underline{x}_3)(w\gamma_3 - \underline{x}_3)\right], & w \neq 0 \\ 2\pi\underline{t}\tilde{\tilde{q}}\exp(-w\underline{x}_3), & w = 0 \end{cases}$$

$$\tilde{\tilde{\varphi}}^{I}_{,33} = \begin{cases} \dfrac{2\pi}{w}\tilde{\tilde{q}}\left[\gamma_1\left(w^2\underline{t} + \dfrac{w\underline{x}_3 + 1}{2}\right) + \gamma_2\left(w^2\underline{t} - \dfrac{w\underline{x}_3 - 1}{2}\right) - w\gamma_4 + \exp(-w\underline{x}_3)(w\underline{x}_3 - 1 - w^2\gamma_3)\right], & w \neq 0 \\ -2\pi\underline{t}\tilde{\tilde{q}}w\exp(-w\underline{x}_3), & w = 0 \end{cases}$$

where

$$\gamma_1 = \exp(w\underline{x}_3)\operatorname{erfc}\left(w\sqrt{\underline{t}} + \frac{\underline{x}}{2\sqrt{\underline{t}}}\right),$$

$$\gamma_2 = \exp(-w\underline{x}_3)\operatorname{erfc}\left(w\sqrt{\underline{t}} - \frac{\underline{x}_3}{2\sqrt{\underline{t}}}\right)$$

$$\gamma_3 = \underline{t}\operatorname{erfc}(w\sqrt{\underline{t}}) - \frac{\sqrt{\underline{t}}\exp(-w^2\underline{t})}{\sqrt{\pi}w} + \frac{\operatorname{erf}(w\sqrt{\underline{t}})}{2w^2},$$

$$\gamma_4 = \frac{2\sqrt{\underline{t}}}{\sqrt{\pi}}\exp\left(-w^2\underline{t} - \frac{\underline{x}_3^2}{4\underline{t}}\right)$$

References

[1] Holm, R., 1967, *Electric Contacts: Theory and Application*, Springer-Verlag, New York.
[2] Johnson, K. L., 1985, *Contact Mechanics*, Cambridge University Press, London.
[3] Carslaw, H. S., and Jaeger, J. C., 1959, *Conduction of Heat in Solids*, Oxford University Press, London.
[4] Gao, J., Lee, S. C., Ai, X., and Nixon, H., 2000, "An FFT-Based Transient Flash Temperature Model for General Three-Dimensional Rough Surface Contacts," ASME J. Tribol., **122**, pp. 519–523.

[5] Lin, J. F., Chung, J. C., Chen, J. W., and Liu, T. C., 2005, "Thermal Analysis of the Transient Temperatures Arising at the Contact Spots of Two Sliding Surfaces," ASME J. Tribol., **127**, pp. 694–704.
[6] Zhai, X. J., and Chang, L., 2000, "A Transient Thermal Model for Mixed-Film Contacts," Tribol. Trans., **43**(3), pp. 427–434.
[7] Green, I., 2002, "A Transient Dynamic Analysis of Mechanical Seals Including Asperity Contact and Face Deformation," Tribol. Trans., **45**(3), pp. 284–293.
[8] Kulkarni, S. M., Rubin, C. A., and Hahn, G. T., 1991, "Elasto-Plastic Coupled Temperature-Displacement Finite Element Analysis of Two-Dimensional Rolling-Sliding Contact With a Translating Heat Source," ASME J. Tribol., **113**, pp. 93–101.
[9] Gupta, V., Bastias, P., Hahn, G. T., and Rubin, C. A., 1993, "Elasto-Plastic Finite-Element Analysis of 2-D Rolling-Plus-Sliding Contact With Temperature-Dependent Bearing Steel Material Properties," Wear, **169**, pp. 251–256.
[10] Ye, N., and Komvopoulos, K., 2003, "Three-Dimensional Finite Element Analysis of Elastic-Plastic Layered Media Under Thermomechanical Surface Loading," ASME J. Tribol., **125**, pp. 52–59.
[11] Wang, Q., and Liu, G., 1999, "A Thermoelastic Asperity Contact Model Considering Steady-State Heat Transfer," Tribol. Trans., **42**(4), pp. 763–770.
[12] Liu, G., Wang, Q., and Liu, S. B., 2001, "A Three-Dimensional Thermal-Mechanical Asperity Contact Model for Two Nominally Flat Surfaces in Contact," ASME J. Tribol., **123**, pp. 595–602.
[13] Simmons, J. G., 1963, "Generalized Formula for the Electrical Tunnel Effect Between Similar Electrodes Separated by a Thin Insulating Film," J. Appl. Phys., **34**(6), pp. 1793–1803.
[14] Dietrich, I., 1952, "Messung des Widerstandes dünner isolierender Schichten zwischen Goldkontakten im Bereich des Tunneleffektes," Z. Phys., **132**, pp. 231–238.
[15] Ruschau, G. R., Yoshikawa, S., and Newnham, R. E., 1992, "Resistivities of Conductive Composites," J. Appl. Phys., **72**(3), pp. 953–959.
[16] Kogut, L., and Komvopoulos, K., 2004, "Electrical Contact Resistance Theory for Conductive Rough Surfaces Separated by a Thin Insulating Film," J. Appl. Phys., **95**(2), pp. 576–585.
[17] Kim, B.-K., Hsieh, K.-T., and Bostick, F. X., 1999, "A Three Dimensional Finite Element Model for Thermal Effect of Imperfect Electric Contacts," IEEE Trans. Magn., **35**(1), pp. 170–174.
[18] Kim, W., Wang, Q., Liu, S., and Asta, M., 2006, "Simulation of Steady and Unsteady State Surface Temperature Under Sliding Imperfect Electrical Contact Between Rough Surfaces," *Proceeding of the 23rd International Conference on Electrical Contacts*, pp. 226–231.
[19] Kim, W., 2006, "Sliding Imperfect Electrical Contact of Engineering Surfaces," Ph.D. thesis, Northwestern University, Evanston, IL.
[20] Liu, S. B., and Wang, Q., 2001, "A Three-Dimensional Thermomechanical Model of Contact Between Non-Conforming Rough Surfaces," ASME J. Tribol., **123**, pp. 17–26.
[21] Liu, S. B., Wang, Q., and Harris, S. J., 2003, "Surface Normal Thermoelastic Displacement in Moving Rough Surface Contacts," ASME J. Tribol., **125**, pp. 862–868.
[22] Liu, S. B., and Wang, Q., 2003, "Transient Thermoelastic Stress Fields in a Half-Space," ASME J. Tribol., **125**, pp. 33–43.
[23] Jacq, C., Nelias, D., Lormand, G., and Girodin, D., 2002, "Development of a Three-Dimensional Semi-Analytical Elastic-Plastic Contact Code," ASME J. Tribol., **124**, pp. 653–667.
[24] Boucly, V., Nelias, D., Liu, S. B., Wang, Q., and Keer, L. M., 2005, "Contact Analyses for Bodies With Frictional Heating and Plastic Behavior," ASME J. Tribol., **127**, pp. 355–364.
[25] Chen, W. W., and Wang, Q., 2008, "Thermomechanical Analysis of Elasto-Plastic Bodies in a Sliding Spherical Contact and the Effects of Sliding Speed, Heat Partition, and Thermal Softening," ASME J. Tribol., **130**, p. 041402.
[26] Nelias, D., Boucly, V., and Brunet, M., 2006, "Elastic-Plastic Contact Between Rough Surfaces: Proposal for a Wear or Running-in Model," ASME J. Tribol., **128**, pp. 236–244.
[27] Boucly, V., Nelias, D., and Green, I., 2007, "Modeling of the Rolling and Sliding Contact Between Two Asperities," ASME J. Tribol., **129**, pp. 235–245.
[28] Nelias, D., Antaluca, E., Boucly, V., and Cretu, S., 2007, "A Three-Dimensional Semianalytical Model for Elastic-Plastic Sliding Contacts," ASME J. Tribol., **129**, pp. 761–771.
[29] Chen, W. W., Wang, Q., Wang, F., Keer, L. M., and Cao, J., 2008, "Three-Dimensional Repeated Elasto-Plastic Point Contacts, Rolling and Sliding," ASME J. Appl. Mech., **75**, pp. 021021.
[30] Ju, Y., and Farris, T. N., 1996, "Spectral Analysis of Two-Dimensional Contact Problems," ASME J. Tribol., **118**, pp. 320–328.
[31] Liu, S. B., Hua, D., Chen, W. W., and Wang, Q., 2007, "Tribological Modeling: Application of Fast Fourier Transform," Tribol. Int., **40**, pp. 1284–1293.
[32] Liu, S. B., Wang, Q., and Liu, G., 2000, "A Versatile Method of Discrete Convolution and FFT (DC-FFT) for Contact Analyses," Wear, **243**, pp. 101–111.
[33] Polonsky, I. A., and Keer, L. M., 1999, "A Numerical Method for Solving Rough Contact Problems Based on Multi-Level Multi-Summation and Conjugate Gradient Techniques," Wear, **231**, pp. 206–219.
[34] Greenwood, J. A., 1966, "Constriction Resistance and the Real Area of Contact," Br. J. Appl. Phys., **17**, pp. 1621–1632.
[35] Liu, S. B., Peyronnel, A., Wang, Q., and Keer, L. M., 2005, "An Extension of the Hertz Theory for Three-Dimensional Coated Bodies," Tribol. Lett., **18**(3), pp. 303–314.
[36] Seo, K., and Mura, T., 1979, "The Elastic Field in a Half Space Due to Ellipsoidal Inclusions With Uniform Dilatational Eigenstrains," ASME J. Appl. Mech., **46**, pp. 568–572.
[37] Liu, S. B., and Wang, Q., 2002, "Studying Contact Stress Fields Caused by Surface Tractions With a Discrete Convolution and Fast Fourier Transform Algorithm," ASME J. Tribol., **124**, pp. 36–45.
[38] Love, A. E. H., 1929, "The Stress Produced in a Semi-Infinite Solid by Pressure on Part of the Boundary," Philos. Trans. R. Soc. London, Ser. A, **228**, pp. 377–420.
[39] Chiu, Y. P., 1978, "On the Stress Field and Surface Deformation in a Half Space With a Cuboidal Zone in Which Initial Strains Are Uniform," ASME J. Appl. Mech., **45**, pp. 302–306.
[40] Lee, W.-S., Sue, W.-C., Lin, C.-F., and Wu, C.-J., 2000, "The Strain Rate and Temperature Dependence of the Dynamic Impact Properties of 7075 Aluminum Alloy," J. Mater. Process. Technol., **100**, pp. 116–122.
[41] Hill, R., 1950, *The Mathematical Theory of Plasticity*, Oxford University Press, London.
[42] Kogut, L., and Etsion, I., 2003, "A Semi-Analytical Solution for the Sliding Inception of a Spherical Contact," ASME J. Tribol., **125**, pp. 499–506.
[43] Kim, B.-K., 1997, "Phenomenological Modeling of Imperfect Electric Contact Using a Three Dimensional Finite Element Model," Ph.D. thesis, University of Texas at Austin, Austin, TX.